Journal of Materials Chemistry C

ROYAL SOCIETY OF CHEMISTRY

PAPER

View Article Online
View Journal

Cite this: DOI: 10.1039/d1tc02668b

An overview of oxygen vacancy dynamics in $(1-x)(Bi_{1/2}Na_{1/2})TiO_3$–$xBaTiO_3$ solid solution

Zhongming Fan * and Clive A. Randall

Received 9th June 2021,
Accepted 13th July 2021

DOI: 10.1039/d1tc02668b

rsc.li/materials-c

$(Bi_{1/2}Na_{1/2})TiO_3$ (BNT) based ceramics have been the hot topic for a few years because of their multiple functions, from the piezoelectric properties to more recently the electrostatic energy storage performance. However, some basic issues are still unclear, preventing their wide application in real devices. One of them is the underlying conduction mechanism, the interplay of electronic and ionic carriers as a mixed ionic case and the subsequent quantification. This paper deals with the most basic compositions, which are the typical ones from the $(1-x)(Bi_{1/2}Na_{1/2})TiO_3$–$xBaTiO_3$ (BNT–xBT) phase diagram. The conductivity is primarily investigated by impedance spectroscopy, while different equivalent circuits are applied to different conduction mechanisms. A transition from predominantly ionic to predominantly electronic conduction is revealed to occur with the increase in $BaTiO_3$ concentration. The mixed ionic–electronic conduction in the composition near the morphotropic phase boundary, namely BNT–7%BT, is identified and then quantified. To verify our interpretation of impedance results, dc degradation is, for the first time, conducted in this family of materials, from which the electronic and ionic conductions can be easily separated by accessing the mean time to failure. The successful combination of the two methods enables us to have an overview of how the oxygen vacancy dynamics in the BNT–xBT system depends upon the phase nature or the domain structure.

1. Introduction

Over the past twenty years there has been dramatic development of lead-free ferroelectric ceramics.[1] So far, the community has recognized several base compositions that deserve extensive investigations, *e.g.* $(K_{1/2}Na_{1/2})NbO_3$ (KNN), $(Bi_{1/2}Na_{1/2})TiO_3$ (BNT), $BaTiO_3$ (BT), $AgNbO_3$ (AN), *etc.*[2–5] Among them, BNT stands out for its multifunctionality: $d_{33} \sim 200$ pC/N is achieved in the morphotropic phase boundary in various solid solutions;[6] a large electro-strain is observed near the depolarization temperature;[7] high levels of ionic conductivity are endowed by acceptor doping;[8] good energy storage density and efficiency are realized in the so-called "relaxor antiferroelectric" phase.[9] Generally speaking, understanding the oxygen vacancy dynamics is of great importance for electroceramics. First, in the case of BNT the high volatility of Bi and Na naturally facilitates the formation of oxygen vacancies during high temperature sintering,[10] while the weak Bi–O bonding gives rise to structural instability and hence provides high oxygen vacancy mobility.[11] Second, the aforementioned properties of BNT always require a prolonged exposure to an electric field, which makes the reliability issue a major concern as oxygen vacancies can electromigrate through the material.

In 2013, Sinclair's group first characterized the excellent ionic conduction in BNT and later on demonstrated the tunability of its conductivity by adding aliovalent dopants or adjusting the Bi/Na stoichiometry.[10,12] They primarily employed electromotive force (EMF) to measure the oxygen ionic transport number and accordingly classified BNT into three types: (I) predominantly ionic conduction; (II) mixed ionic–electronic conduction; and (III) predominantly electronic conduction.[13] Regular BNT belongs to type I. With the addition of a subtle amount of the Nb^{5+} donor or excess Bi, BNT evolves to type II. It eventually becomes type III with further addition.[12] Compared with pure BNT, BNT-based solid solutions are more widely used.[6] Unless being doped with acceptors, common binary/ternary solid solutions are always claimed to be type III where a single semicircle in Impedance Spectroscopy (IS) is interpreted as electronic conduction.[14] However, the interconnection of type I to III transition is not appreciated with respect to the phase diagram of a solid solution.

The objective of this work is to further investigate the composition dependence of the conduction mechanism across the phase diagram. In this paper, we are employing a dedicated equivalent circuit that can readily separate the ionic and electronic contributions to the total conductivity in IS. A critical concern immediately arises whether our interpretation is valid and sufficient, relative to the methods used earlier on the ionic conductivity of BNT, namely, EMF and tracer diffusion. Here we further employ a dc degradation to potentially serve as a solid evidence. DC degradation is a process in which the oxygen vacancies migrate towards the cathodic blocking electrode

Materials Research Institute, Pennsylvania State University, University Park, Pennsylvania 16802, USA. E-mail: zbf5066@psu.edu

under a constant electric bias, accompanied by an increase of leakage current.[15] Thus, the activation energy for oxygen vacancy migration can be known as it governs the degradation process. The standard method is Highly Accelerated Lifetime Test (HALT) where a constant bias is applied at different elevated temperatures.[16] The mean time to failure (MTTF), namely, the moment when the leakage current takes off, is defined as when the leakage current increases by a factor of ten. Knowing this, the activation energy can be calculated by fitting MTTF data to the Eyring equation:

$$\frac{t_1}{t_2} = \left(\frac{V_2}{V_1}\right)^n \exp\left[\frac{E_a}{k}\left(\frac{1}{T_1} - \frac{1}{T_2}\right)\right], \quad (1)$$

where t_i is the MTTF under electric bias V_i at temperature T_i, E_a is the activation energy, k is the Boltzmann constant, and n is the voltage acceleration factor. For a given voltage, eqn (1) reduces to the Arrhenius model:

$$\frac{t_1}{t_2} = \exp\left[\frac{E_a}{k}\left(\frac{1}{T_1} - \frac{1}{T_2}\right)\right]. \quad (2)$$

The solid solution we choose to study is the most classic one, $(1-x)(Bi_{1/2}Na_{1/2})TiO_3$–$xBaTiO_3$ (BNT–xBT). Fig. 1 displays a simplified phase diagram.[17] Pure BNT is *R3c* phase, despite that some researchers believe it to be *Cc*.[18] The morphotropic phase boundary resides in the range from x = 6% to 11%. The highest d_{33} ~ 180 pC/N is seen in BNT–7%BT, attributed to the coexistence of *R3c* and *P4bm* phases. Further to the right, BNT–15%BT has entered the *P4mm* phase region. The corresponding dielectric measurements are inserted in the phase diagram. Both pure BNT and BNT–7%BT feature obvious frequency dispersion at low temperatures, whereas BNT–15%BT shows just a slight dispersion. In this work, we examine the oxygen vacancy dynamics in these three typical compositions, systematically.

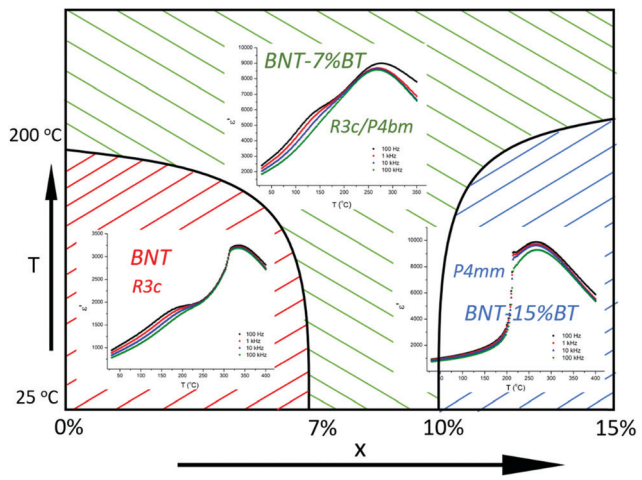

Fig. 1 Phase diagram of BNT–xBT. The dielectric constants measured in the unpoled state of the three studied compositions, pure BNT, BNT–7%BT and BNT–15%BT, are shown as insets.

2. Experimental

The pure BNT, BNT–7%BT, BNT–15%BT and BNT–15%BT–1%Ga ceramics were fabricated using the conventional solid state reaction method, with starting powders of Bi_2O_3 (>99.9%), Na_2CO_3 (>99.95%), TiO_2 (>99.9%), $BaCO_3$ (>99.8%) and Ga_2O_3 (>99.99%) weighed according to the stoichiometry. The mixed powders were ball-milled in ethanol for 24 hours both before and after being calcined at 850 °C for 2 hours. The sintering was carried out at 1150–1200 °C for 2 hours with the green pellet unburied by any protective powder. The sintered ceramics were slowly cooled down with a furnace to avoid any quenching effects that have been found to be able to increase the conductivity in BNT. The as-sintered pellets were polished to ~1 mm thickness before platinum electrodes were sputtered. The IS was performed in a computer-controlled furnace with a Solartron ModuLab XM impedance analyzer from 0.1 Hz to 1 MHz. The HALT was conducted by applying a constant electric bias to the ceramics at elevated temperatures, while the leakage current was read using a digital multimeter (Keithley 2700). The domain structure of the ceramics was checked using Transmission Electron Microscopy (TEM) on a Talos F200X (FEI). The TEM specimens were prepared by ion milling (PIPS II, Gatan), followed by annealing at 500 °C to remove any possible impacts from the thermal history.

3. Results and discussion

The impedance of pure BNT is relatively straightforward to analyze, but here we use it matching IS and HALT data, to understand the transient changes as degradation proceeds. Following Sinclair,[10] we use two resistor-constant phase elements (R-CPE) that respectively represent the grain and grain boundary, connected in series to perfectly fit the two semicircles in IS (Fig. 2a and b). The Arrhenius plot of the grain conductivity is shown in Fig. 2c and the activation energy is ~0.87 eV, suggesting the ionic conduction. HALT is done on pure BNT at 100, 125 and 150 °C under 3 kV cm^{-1} (Fig. 2d). Initially, the current rises slowly. Subsequently, the increase of the current becomes more rapid until it slows down again. Eventually, a plateau is reached. Such a re-stabilization of the conductivity is commonly observed in acceptor doped perovskites during dc degradation, which is ascribed to the redox reactions that take place within the cathodic/anodic layer.[19] We have noted that the reduction is not just at the interface, and the depth has variations with different compositions. We will present a detailed discussion regarding this in a separate paper. The short arrows in Fig. 2d mark the MTTFs at different temperatures, which are then fitted according to eqn (2) in Fig. 2e. The activation energy is calculated to be ~ 0.85 eV, in good agreement with the value obtained from IS (Fig. 2c). Several things can be concluded here: first, pure BNT indeed features predominantly ionic conduction (type I) due to the high concentration/mobility of oxygen vacancies; second, the dc degradation in pure BNT is governed by the electromigration of oxygen vacancies, inferred by the activation energy; third, HALT turns out to be a convenient way to extract the ionic

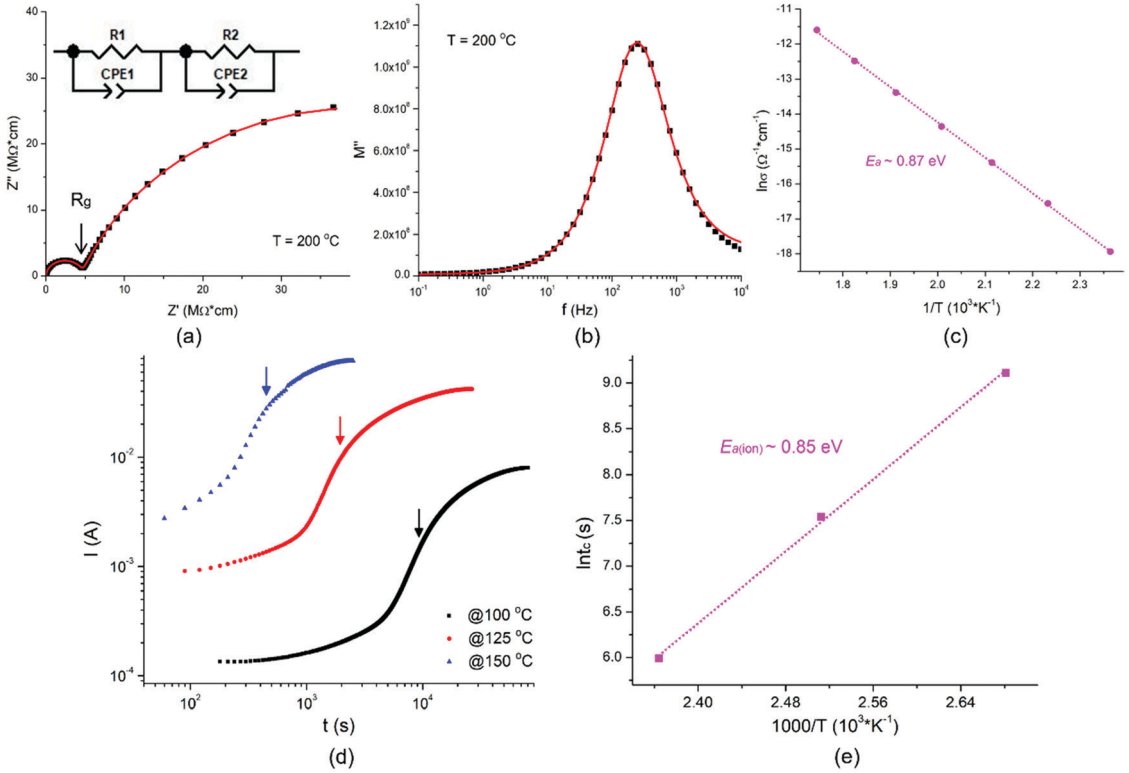

Fig. 2 Electrical measurements in pure BNT. (a) Fitting of the Z^* plot using the equivalent circuit in the inset; (b) replotting of the fitting result in $M''(f)$; (c) Arrhenius fitting of the grain conductivity; (d) HALT at different temperatures, with the MTTFs marked by small arrows; and (e) Arrhenius fitting of the MTTFs (denoted as t_c).

conductivity, if any, from the total conductivity, therefore providing a powerful tool for studying mixed conduction (type II) in combination with IS.

Similar investigations are carried out in BNT–7%BT. The Z^* plot in Fig. 2a shows only one semicircle, which has been interpreted as the bulk resistance. However, unlike pure BNT, the semicircle in BNT–7%BT is so distorted that a single R-CPE cannot generate a satisfactory fitting result. Note that if Arrhenius fitting is done with the bulk resistance that is simply extracted from the intercept of the Z' axis, we can still obtain an activation energy. However, the mixed conductivities can by no means be easily separated. In order to reveal the distortion in the semi-circle more clearly, impedance is replotted in the electric modulus formalism, $M^* = j\omega C_0 Z^*$. As can be seen in Fig. 3b, $M''(f)$ is asymmetric due to an obvious "shoulder" at a high frequency. It should be noted that we are not the first group to discover such a "shoulder" in BNT-based solid solutions. Previously, this shoulder was attributed to an additional dielectric relaxation of the polar nanoregions, indicated by the successful fitting to the Vogel–Fulcher rather than Arrhenius equation.[20] Here we propose an alternative interpretation, the "shoulder" originates from ionic conduction. Given that ionic species are blocked at the electrode, while the electronic species are permeable at the electrode, the ionic and electronic conductions are then separable.[21–24] The equivalent circuit we used here is composed of three rails: the first rail represents the electronic resistance R_e; the second rail is the bulk capacitance C_1; the third rail consists of the series connection of the ionic resistance and the interface capacitance R_i-CPE$_1$. At a high frequency, the ionic rail is conductive and hence the total resistance is $(R_e^{-1} + R_i^{-1})^{-1}$. At a low frequency, the ionic species have time to accumulate at the electrode and the impedance approaches R_e in the dc limit. Fig. 3c displays the temperature dependence of the electronic and ionic conductivity, of which the activation energies are $E_{a\,(ion)} \sim 0.76$ eV and $E_{a\ (ele)} \sim 1.08$ eV, respectively. To verify our interpretation and results, HALT is done at 200, 225, 250 °C under 5 kV cm^{-1} (Fig. 3d). Similar to the pure BNT, the leakage current in BNT–7%BT increases with time, first slowly and then rapidly. However, an important difference from pure BNT is the absence of a plateau (note that the horizontal tails are because of the current limit of the system). As explained above, the conductivity re-stabilization is often seen in acceptor doped perovskites that have sufficient ionic electromigration to induce dramatic redox reactions near the electrodes, which is not the case in BNT–7%BT as a mixed conductor. Nevertheless, in the BNT–7%BT doped with acceptor dopants, the ionic conduction becomes predominant, while the impedance data are qualitatively identical to those of pure BNT.[14] In those compositions, a plateau appears in the final stage of degradation. This will be discussed in more detail in a separate paper. The activation energy of ionic conduction is calculated, by fitting the MTTFs (marked by the small arrows), to be ~0.76 eV. In terms of the dc conductivity (electronic), the

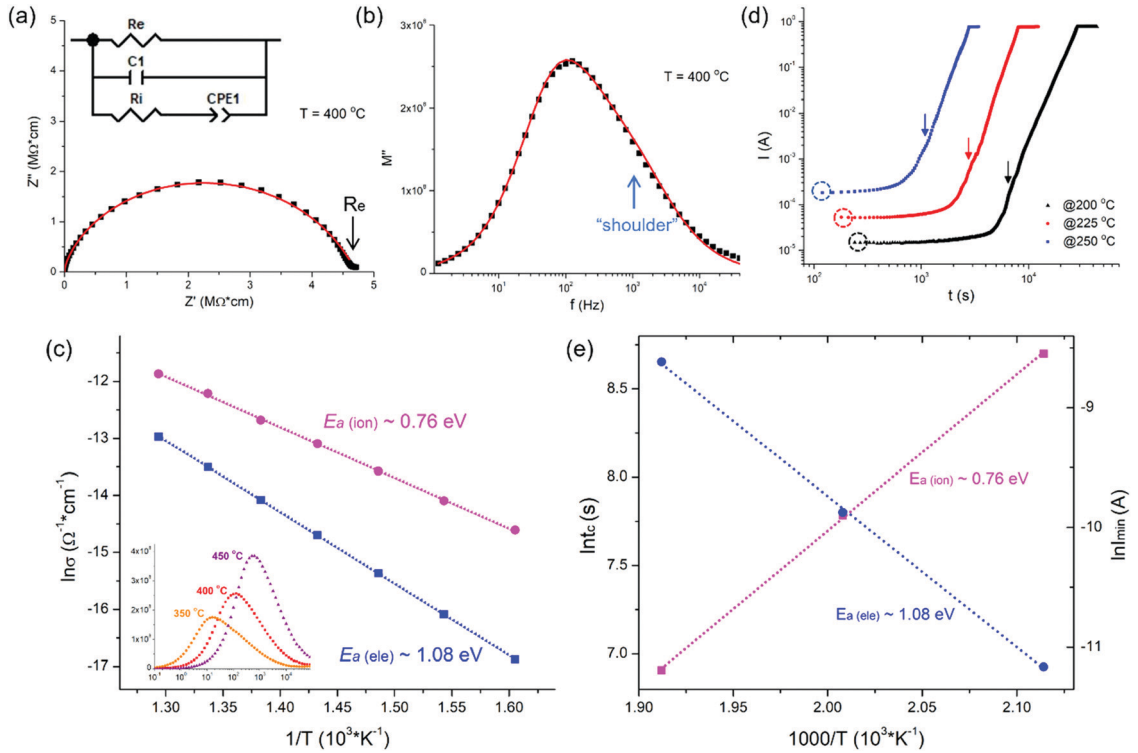

Fig. 3 Electrical measurements in BNT–7%BT. (a) Fitting of the Z^* plot using the equivalent circuit in the inset; (b) replotting of the fitting result in $M''(f)$; (c) Arrhenius fitting of the ionic and electronic conductivities; the inset shows the modulus at three different temperatures; (d) HALT at different temperatures, with the MTTFs marked by small arrows and the initial leakage currents marked by small circles; and (e) Arrhenius fitting of the MTTFs and the initial leakage currents.

initial leakage currents (marked by the small circles) are accessed through

$$J = J_0 \exp\left[\frac{-E_a}{kT}\right], \quad (3)$$

while the activation energy is ~1.08 eV (Fig. 3e). Both values are exactly the same as the ones obtained from IS, indicating that our selection of equivalent circuit and the fitting results are valid. On the other hand, in the acceptor doped BNT–7%BT (type I), the activation energy for the ionic conduction, obtained by fitting with the two R-CPE equivalent circuits (Fig. 2), lies in the range of 0.75–0.79 eV, which also shows that our result (~0.76 eV) in the undoped case is reasonable. In the Ta^{5+} doped BNT–7%BT (type III), the "shoulder" disappears and $M''(f)$ is symmetric. This again supports our interpretation that the "shoulder" originates from ionic conduction which will be greatly suppressed by donor doping.

Fig. 4 examines the case of BNT–15%BT. The undistorted semi-circle and the symmetric $M''(f)$ with the absence of any "shoulder" along with an activation energy of ~1.40 eV suggest BNT–15%BT to be a type III predominantly electronic conductor with nearly intrinsic semiconducting behavior (Fig. 4a–c). The lower activation energy for the electronic conduction in BNT–7%BT should be due to its relatively larger defect concentration. So far, a type I (ionic) to type II (mixed) to type III (electronic) transition has been completely identified in the BNT–xBT solid solution. However, if we still want to learn more about the oxygen vacancy dynamics in BNT–15%BT, we need to add acceptor dopants to make it type I. Fig. 4d is the dielectric constant measured in BNT–15%BT–1%Ga, from which we learn that the phase nature of BNT–15%BT–1%Ga is unchanged compared with the undoped BNT–15%BT (inset of Fig. 1). They both are ferroelectric at low temperatures and relaxors at high temperatures, even when the phase transition temperatures are the same, ~ 210 °C. The impedance of BNT–15%BT–1%Ga appears to be analogous to that of pure BNT and is therefore analyzed using the same method. The Arrhenius plot has two regimes with distinct activation energies, ~0.93 eV below 210 °C and ~0.72 eV above 210 °C (Fig. 4e). 0.93 eV is never seen in any composition above, but 0.72 eV is very close to the value in BNT–7%BT. Therefore, this suggests that the oxygen vacancy dynamics in BNT is dependent upon the phase nature.

To extend the discussion, let us first summarize the activation energies for oxygen vacancy migration that we have obtained so far. The smallest E_a values (<0.8 eV) are found in BNT–7%BT and BNT–15%BT above the ferroelectric to relaxor transition temperature; the intermediate E_a (between 0.8 and 0.9 eV) is found in pure BNT; the largest E_a (>0.9 eV) is found in BNT–15%BT below the transition temperature. It can be seen from the phase diagram (Fig. 1) that pure BNT is *R3c* phase, BNT–7%BT is on the *R3c*/*P4bm* phase boundary, and BNT–15%BT is also *P4bm* phase at a high temperature and is *P4mm* at a low temperature. Meyer *et al.* used DFT calculations to show that the oxygen vacancy migration barriers are different

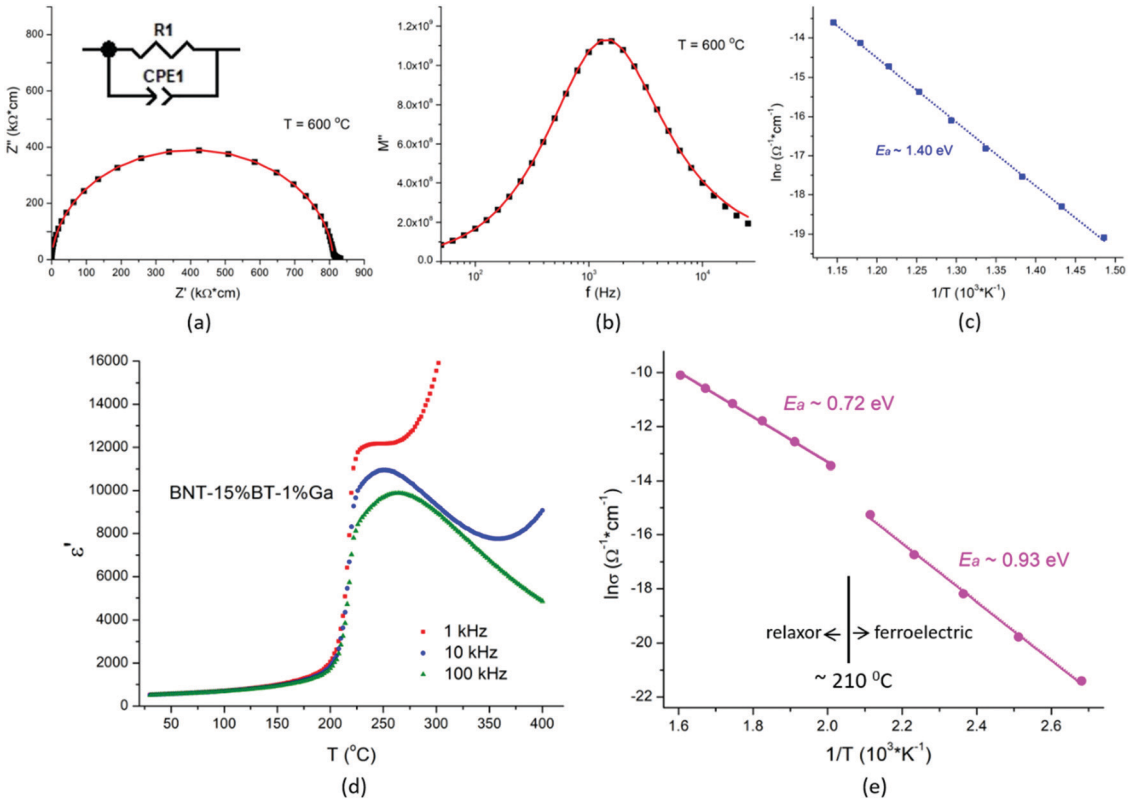

Fig. 4 Electrical measurements in BNT–15%BT. (a) Fitting of the Z^* plot using the equivalent circuit in the inset; (b) replotting of the fitting result in $M''(f)$; (c) Arrhenius fitting of the conductivity of BNT–15%BT; (d) temperature dependent dielectric constant in BNT–15%BT–1%Ga; and (e) Arrhenius fitting of the bulk conductivity of BNT–15%BT–1%Ga.

in rhombohedral, orthorhombic and tetragonal phases in BNT.[25] Our systematic investigation in the BNT–xBT solid solution leads to a similar conclusion, $E_{a\,(P4mm)} > E_{a\,(R3c)} > E_{a\,(P4bm)}$ (Fig. 5). Another possible cause is related to the changes in the domain structure. The grains in BNT–15%BT are full of large twinned ferroelectric domains of lamellar shape (Fig. 5a). The domain morphology in pure BNT was always described as ''complex domains'' (Fig. 5b).[26] In fact, the complexity results from the coexistence of smaller ferroelectric domains and dense antiphase boundaries. BNT–7%BT features polar nanoregions instead of normal ferroelectric domains (Fig. 5c), and such a microstructure presumably dominates in BNT–15%BT after the ferroelectric domains vanish above the transition temperature. It is well known that the ferroelectric domain walls are often not completely neutralized, which gives rise to an electrostatic interaction with the positively charged oxygen vacancy.[27,28] Once an oxygen vacancy is trapped at a well-defined ferroelectric domain wall, it requires more energy to hop out, namely, a higher activation energy, as modelled earlier by Cao *et al.*[29] In the relaxor phase, on the contrary, the ferroelectric domains are disrupted so that the ''blocking'' force from the domain wall might become weaker, which makes the

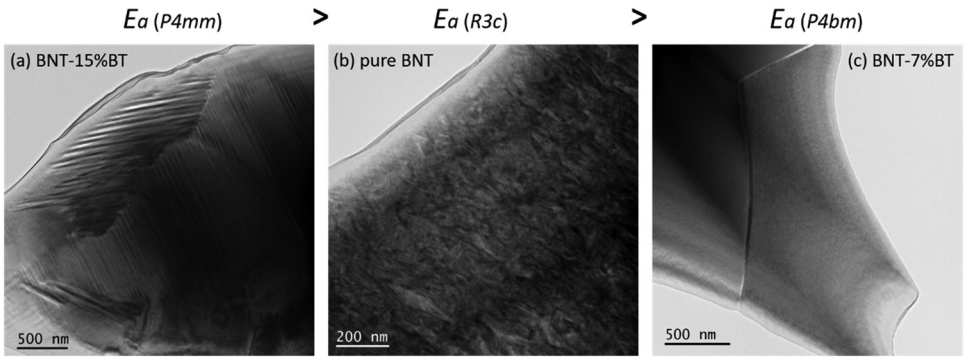

Fig. 5 The domain morphology in (a) BNT–15%BT; (b) pure BNT; and (c) BNT–7%BT. E_a is the activation energy for oxygen vacancy migration in each composition.

ionic hopping easier so that the activation energy drops. However, whether the polar nanoregions or other microstructural entities in BNT-based relaxors exert an additional barrier to the ionic hopping is currently under investigation.

4. Conclusions

The oxygen vacancy dynamics is systematically examined in the BNT–*x*BT solid solution. A transition from ionic conductor through mixed conductor to electronic conductor is determined as *x* increases from 0 (<MPB) through 7% (=MPB) to 15% (>MPB). The ionic and electronic conductivities in BNT–7%BT are separated using a dedicated equivalent circuit. More importantly, such an interpretation is validated by the DC degradation study, which is demonstrated to be an easy way to extract the ionic contribution from the total conduction. Therefore, the comparison of oxygen vacancy dynamics in different phases/domain structures is made possible. The activation energy for oxygen vacancy migration is, from the largest to the smallest, *P*4*mm*/big ferroelectric domains, *R*3*c*/complex domains and *P*4*bm*/polar nanoregions.

Conflicts of interest

There are no conflicts to declare.

Acknowledgements

This work was supported by the National Science Foundation, as part of the Center for Dielectrics and Piezoelectrics, under Grant No. IIP-1841453 and 1841466.

References

1 J. Rödel, W. Jo, K. Seifert, E. Anton, T. Granzow and D. Damjanovic, *J. Am. Ceram. Soc.*, 2009, **92**, 1153–1177.
2 Y. Saito, H. Takao, T. Tani, T. Nonoyama, K. Takatori, T. Homma, T. Nagaya and M. Nakamura, *Nature*, 2004, **432**, 84–87.
3 G. O. Jones and P. A. Thomas, *Acta Crystallogr., Sect. B: Struct. Sci.*, 2002, **58**, 168–178.
4 W. Liu and X. Ren, *Phys. Rev. Lett.*, 2009, **103**, 257602.
5 H. U. Khan, K. Alam, M. Mateenullah, T. Blaschke and B. S. Haq, *J. Eur. Ceram. Soc.*, 2015, **35**, 2775–2789.
6 Y. Hiruma, H. Nagata and T. Takenaka, *J. Appl. Phys.*, 2008, **104**, 124106.
7 W. Jo, T. Granzow, E. Aulbach, J. Rödel and D. Damjanovic, *J. Appl. Phys.*, 2009, **105**, 094102.
8 F. Yang, M. Li, L. Li, P. Wu, E. Pradal-Velázque and D. C. Sinclair, *J. Mater. Chem. A*, 2017, **5**, 21658–21662.
9 J. Li, F. Li, Z. Xu and S. Zhang, *Adv. Mater.*, 2018, **30**, 1802155.
10 M. Li, M. J. Pietrowski, R. A. De Souza, H. Zhang, I. M. Reaney, S. N. Cook, J. A. Kilner and D. C. Sinclair, *Nat. Mater.*, 2014, **13**, 31–35.
11 D. Schütz, M. Deluca, W. Krauss, A. Fetira, T. Jackson and K. Reichmann, *Adv. Funct. Mater.*, 2002, **22**, 2285–2294.
12 L. Li, M. Li, H. Zhang, I. M. Reaney and D. C. Sinclair, *J. Mater. Chem. C*, 2016, **4**, 5779–5786.
13 L. Li, M. Li, I. M. Reaney and D. C. Sinclair, *J. Mater. Chem. C*, 2017, **5**, 6300–6310.
14 S. Steiner, I. Seo, P. Ren, M. Li, D. J. Keeble and T. Frömling, *J. Am. Ceram. Soc.*, 2019, **102**, 5295–5304.
15 R. Waser, T. Baiatu and K. Härdtl, *J. Am. Ceram. Soc.*, 1990, **73**, 1645–1653.
16 S. Zhao, S. J. Zhang, W. Liu, N. J. Donnelly, Z. Xu and C. A. Randall, *J. Appl. Phys.*, 2009, **105**, 053705.
17 C. Ma, X. Tan, E. Dul'kin and M. Roth, *J. Appl. Phys.*, 2010, **108**, 104105.
18 C. Ma, H. Guo and X. Tan, *Adv. Funct. Mater.*, 2013, **23**, 5261–5266.
19 R. Waser, T. Baiatu and K. Härdtl, *J. Am. Ceram. Soc.*, 1990, **73**, 1654–1662.
20 J. Zang, M. Li, D. C. Sinclair, T. Frömling, W. Jo and J. Rödel, *J. Am. Ceram. Soc.*, 2014, **97**, 2825–2831.
21 N. J. Donnelly and C. A. Randall, *Appl. Phys. Lett.*, 2010, **96**, 052906.
22 J. Jamnik and J. Maier, *Phys. Chem. Chem. Phys.*, 2011, **3**, 1668–1678.
23 J. Jamnik and J. Maier, *J. Electrochem. Soc.*, 1999, **146**, 4183.
24 C. Slouka, G. Holzlechner, L. Andrejs, E. Navickas, H. Hutter and J. Fleig, *J. Am. Ceram. Soc.*, 2015, **98**, 3259–3269.
25 K. Meyer and K. Able, *J. Mater. Chem. A*, 2017, **5**, 4368–4375.
26 H. Qi, R. Zuo, X. Zhou and D. Zhang, *J. Alloys Compd.*, 2019, **802**, 6–12.
27 C. Paillard, G. Geneste, L. Bellaiche and B. Dkhil, *J. Phys.: Condens. Matter*, 2017, **29**, 485707.
28 Z. Fan, S. Zhang and X. Tan, *J. Eur. Ceram. Soc.*, 2020, **40**, 1217–1222.
29 Y. Cao, J. Shen, C. A. Randall and L. Q. Chen, *Acta Mater.*, 2016, **112**, 224–230.

